

# Journal of Materials Chemistry A

Accepted Manuscript



This is an *Accepted Manuscript*, which has been through the Royal Society of Chemistry peer review process and has been accepted for publication.

*Accepted Manuscripts* are published online shortly after acceptance, before technical editing, formatting and proof reading. Using this free service, authors can make their results available to the community, in citable form, before we publish the edited article. We will replace this *Accepted Manuscript* with the edited and formatted *Advance Article* as soon as it is available.

You can find more information about *Accepted Manuscripts* in the [Information for Authors](#).

Please note that technical editing may introduce minor changes to the text and/or graphics, which may alter content. The journal's standard [Terms & Conditions](#) and the [Ethical guidelines](#) still apply. In no event shall the Royal Society of Chemistry be held responsible for any errors or omissions in this *Accepted Manuscript* or any consequences arising from the use of any information it contains.

# Novel Understanding of Carbothermal Reduction Enhancing Electronic and Ionic Conductivity of $\text{Li}_4\text{Ti}_5\text{O}_{12}$ Anode

Bo Yan,<sup>a, b, c</sup> Minsi Li,<sup>d</sup> Xifei Li,<sup>\*b</sup> Zhimin Bai,<sup>\*a</sup> Jianwen Yang,<sup>\*c</sup> Dongbin Xiong,<sup>b</sup>  
Dejun Li<sup>b</sup>

<sup>a</sup>*Beijing Key Laboratory of Materials Utilization of Nonmetallic Minerals and Solid Wastes, National Laboratory of Mineral Materials, School of Materials Science and Technology, China University of Geosciences, Beijing, 100083. E-mail: [zhimibai@cugb.edu.cn](mailto:zhimibai@cugb.edu.cn); Tel: +86-13691115187*

<sup>b</sup>*Energy & Materials Engineering Centre, College of Physics and Materials Science, Tianjin Normal University, Tianjin 300387, China. E-mail: [xfli2011@hotmail.com](mailto:xfli2011@hotmail.com); Tel: +86-22-23766526, Fax: +86-22-23766503*

<sup>c</sup>*College of Chemistry and Bioengineering, Guilin University of Technology, Guilin, 541004, China. E-mail: [yangjw@glite.edu.cn](mailto:yangjw@glite.edu.cn); Tel: +86-773-5896446*

<sup>d</sup>*CAS Key Laboratory of Materials for Energy Conversion, Department of Materials Science and Engineering, University of Science and Technology of China, Anhui, Hefei 230026, P. R. China*

## Abstract

Spinel  $\text{Li}_4\text{Ti}_5\text{O}_{12}$  performance highly depends on both electronic and ionic conductivity, and however, developing a low-cost strategy to improve its electronic and ionic conductivity still remains challenging. In this study, a facile cost-saving carbothermal reduction method is introduced to synthesize the microscaled spinel

$\text{Li}_4\text{Ti}_5\text{O}_{12}$  particles with surface modification of Ti(III) using anatase- $\text{TiO}_2$ ,  $\text{Li}_2\text{CO}_3$ , and acetylene black (AB) as precursors. Remarkably, this ingenious design can easily eliminate the influence of the residual carbon, and thus make it possible to individually study the effect of Ti(III) on bulk  $\text{Li}_4\text{Ti}_5\text{O}_{12}$ . To reveal the role of Ti(III), the electronic conductivity and lithium-ion diffusion coefficient of the as-prepared materials were measured using direct volt-ampere method, electrochemical impedance spectroscopy (EIS), and cyclic voltammetry (CV). The results indicate that the carbothermal reduction leads to increased electronic and ionic conductivity of the spinel  $\text{Li}_4\text{Ti}_5\text{O}_{12}$ . As a result, the modified  $\text{Li}_4\text{Ti}_5\text{O}_{12}$  exhibits enhanced cyclic stability, improved rate capability, and high Coulombic efficiency. The carbothermal reduction mechanism discreetly clarified in this study is beneficial of improving  $\text{Li}_4\text{Ti}_5\text{O}_{12}$  performance for further commercial applications.

## 1. Introduction

Lithium ion batteries (LIBs) have been regarded as one of the most promising candidates for applications in the coming era of electric and hybrid vehicles with the potential to save fossil fuels and reduce carbon dioxide.<sup>1-4</sup> However, the large-scale application of the lithium-ion battery technology will highly depend on the cost, safety, and service life, which are in turn controlled by the component materials used.<sup>5</sup> <sup>6</sup> Graphite material is commonly used as an anode in commercial LIBs, but exhibits poor rate performance due to its low Li diffusion coefficient and serious safety issues

because of potential solid electrolyte interphase (SEI) film formation.<sup>7-10</sup> Therefore, some advanced materials with excellent rate and better safety capability are critical components for the next generation of LIBs.

As an alternative material to graphite anode, the spinel  $\text{Li}_4\text{Ti}_5\text{O}_{12}$  has been extensively studied as an ideal material for large-scale LIBs because its Li-insertion process operates at around 1.5 V (*versus*  $\text{Li}/\text{Li}^+$ ), ensuring much better safety characteristics by avoiding the formation of dendritic lithium.<sup>11, 12</sup> Furthermore, spinel  $\text{Li}_4\text{Ti}_5\text{O}_{12}$  shows a negligible volume variation during the lithium intercalation-deintercalation process, consequently resulting in a long cycling lifetime.<sup>11-13</sup> Unfortunately, the rate performance of bulk  $\text{Li}_4\text{Ti}_5\text{O}_{12}$  is greatly limited due to the poor electronic and ionic conductivity, which constitutes a major obstacle for its large-scale applications.<sup>14-16</sup> Therefore, to improve the rate capability of  $\text{Li}_4\text{Ti}_5\text{O}_{12}$ , a number of strategies, including carbon coating,<sup>16, 17</sup> metal or nonmetal ion doping,<sup>14, 15, 18</sup> hybridization with graphene or metal powders,<sup>19-22</sup> and reduction in particle size,<sup>10, 20, 23</sup> have been addressed to realize this purpose and have yielded a variety of notable results. However, all these suffer from the difficulties in rational handling due to the complicated procedures, and are thus not in favor of practical applications. Undoubtedly, the facile synthesis of  $\text{Li}_4\text{Ti}_5\text{O}_{12}$  with simultaneously improved the electronic and ionic conductivity still remains challenging.

Normally, the  $\text{Li}_4\text{Ti}_5\text{O}_{12}$  anode exhibits a two-phase electrochemical process with lithium, resulting in an obvious plateau. It is important to note that the solid solution  $\text{Li}_{4+\delta}\text{Ti}_5\text{O}_{12}$  (or  $\text{Li}_{7-\gamma}\text{Ti}_5\text{O}_{12}$ ) resulting from mixed-valent  $\text{Ti}^{3+}/\text{Ti}^{4+}$  appears in the

insertion/extraction process of  $\text{Li}_4\text{Ti}_5\text{O}_{12}$ ,<sup>24,25</sup> which is similar to the electrochemical process of  $\text{LiFePO}_4$ .<sup>26</sup> More significantly, the solid solution (solid solution = single-phase insertion/extraction) phenomenon existing in the electrochemical process of  $\text{Li}_4\text{Ti}_5\text{O}_{12}$  has drawn growing interests since it had been briefly proved that this effect is beneficial for enhancing the rate capacity. For example, Park et al. studied the  $\text{Li}_4\text{Ti}_5\text{O}_{12}$  anode with surface modification of TiN (including Ti(III)) in 2008.<sup>8</sup> The authors gave a primary conclusion that the increase of solid solution can effectively improve the  $\text{Li}_4\text{Ti}_5\text{O}_{12}$  performance. Shortly after that, Zhou et al. developed nano-sized  $\text{Li}_4\text{Ti}_5\text{O}_{12}$  with double surface modifications of Ti(III) and carbon, and only with the EIS results confirmed that the Li-ion diffusion coefficient within the single-phase region is much higher than that of the two-phase region.<sup>27</sup> Very recently, Shao et al. studied TiN-modified  $\text{Li}_4\text{Ti}_5\text{O}_{12}$  with introduction of a small amount of Ti(III) through one-step ammonia reduction synthesis, which also obtained excellent electrochemical performance.<sup>28</sup> However, these previous studies have always focused on the double surface modifications, rather than considering the Ti(III) alone. The real role of Ti(III) with the increase of solid solution in relation to the achieved high rate performance was obscured by the effect of TiN or carbon. More importantly, some obvious difficulties still existed in studying the effect of Ti(III) on  $\text{Li}_4\text{Ti}_5\text{O}_{12}$  anode, such as material preparation. In addition, how Ti(III) affects electronic and ionic conductivity of  $\text{Li}_4\text{Ti}_5\text{O}_{12}$  anode has not been completely illustrated in detail.

Herein, we introduce a cheap one-step solid-state carbothermal reduction method to synthesize  $\text{Li}_4\text{Ti}_5\text{O}_{12}$  with surface modification of Ti(III). More strikingly, this

primitive design can handily eliminate the influence of carbon. Furthermore, in order to further clarify the role of Ti(III), the electrochemical properties of this modified material are studied in detail in comparison to the bulk  $\text{Li}_4\text{Ti}_5\text{O}_{12}$ . It was found that the carbothermal reduction method may be an ideal choice for facile synthesis of  $\text{Li}_4\text{Ti}_5\text{O}_{12}$  with simultaneously improved the electronic and ionic conductivity, thus observably decreasing electrochemical polarization and improving the rate performance of the obtained material.

## 2. Experimental

Surface modified  $\text{Li}_4\text{Ti}_5\text{O}_{12}$  (denoted as LTO-B) powder can be conveniently synthesized by a cost-effective one-step carbothermal reduction method. In a typical synthesis, 0.72 g  $\text{Li}_2\text{CO}_3$ , 1.61 g  $\text{TiO}_2$  and 0.0412 g acetylene black were thoroughly mixed by agate mortar at ambient temperature. Due to the easy evaporation of lithium ions during heating treatment, a little excess of  $\text{Li}_2\text{CO}_3$  was added to the reactants. After that, the above-mentioned mixtures were transferred in tube furnace and sintered at 850 °C for 12 h in the flow argon with heating rate of 5 °C  $\text{min}^{-1}$ , and then cooled down to room temperature naturally in the furnace. For comparison, the pristine  $\text{Li}_4\text{Ti}_5\text{O}_{12}$  (denoted as LTO-W) was synthesized under the similar conditions but treated in air.

X-ray diffraction (XRD) data of LTO-W and LTO-B samples were collected on a X' Pert PRO diffractometer (with Cu  $K\alpha$  radiation of  $\lambda=1.5405 \text{ \AA}$ ) for  $2\theta$  in the range

10°-70°. The lattice parameters were calculated by a least-squares method. The amount of residual carbon (AB) in the LTO-B sample was estimated using a SDTQ600 thermogravimetric analysis/differential scanning calorimetry (TGA/DSC) system from 25–850 °C at 5 °C min<sup>-1</sup> under air atmosphere. The morphologies of the samples were observed using scanning electron microscopy (SEM, JSM-5610LV) under 10 kV accelerating voltage. The microstructure and micro-area chemical composition of the samples were studied by transmission electron microscopy (TEM, JEOL JEM-2100F) operating at 200 kV. The X-ray photoelectron spectroscopy (XPS) analysis of the samples were performed on an Amicus spectrometer (SHIMADZU) with Al K $\alpha$  (1486.8 eV) as the X-ray source. The DC electrical conductivities were measured by a direct volt–ampere method (RST-9, 4 Probes Tech Co.), in which disk samples were contacted with a four-point probe.

The working electrodes were fabricated by blending LTO-W or LTO-B as the active materials, acetylene black (AB) as conductive agent, and polyvinylidene fluoride binder in a weight ratio of 80:10:10 in N-methyl pyrrolidinone. The resultant slurry was spread uniformly on an aluminum foil, and dried overnight in a vacuum at 80 °C. Subsequently, the electrodes were punched in the 14 mm diameter disks, and the typical active electrode loading was about 3.0 mg cm<sup>-2</sup>. The electrochemical performances of these working electrodes were evaluated in a 2025 coin-type cell, in which the lithium foil was used as the counter electrode and reference electrode, the porous polypropylene as the separator, and 1M LiPF<sub>6</sub> in ethylene carbonate (EC), dimethyl carbonate (DMC), and ethylene methyl carbonate (EMC) (1:1:1 by volume)

as the electrolyte. The test cells were assembled in an Ar-filled dry glove box. The electrochemical measurements, including galvanostatic charge-discharge, cyclic voltammetry (CV), and electrochemical impedance spectroscopy (EIS) were performed using a Land CT2001 battery tester or a CHI660D electrochemical workstation. Galvanostatic charge/discharge cycles were performed in the voltage range of 1.0–2.5 V at different current rates (1 C=170 mA g<sup>-1</sup>). The CV curves of the test cells were recorded in a potential range of 0.8–3.0 V (vs Li/Li<sup>+</sup>) at different scan rates. The EIS spectra were systematically measured under prescribed discharge voltage with the frequency ranging from 100 kHz to 10 mHz and an AC signal of 5 mV in amplitude as the perturbation.

### 3. Results and Discussion

#### 3.1. General characterization of the prepared materials

Fig. 1 (a) shows the XRD patterns of the LTO-W and LTO-B samples. The diffraction peaks of both samples consistent with the cubic spinel phase, Li<sub>4</sub>Ti<sub>5</sub>O<sub>12</sub> (space group Fd3m (227), JCPDS No. 47-0207), were observed, and the cubic crystalline structure of spinel Li<sub>4</sub>Ti<sub>5</sub>O<sub>12</sub> is presented in Fig. 1 (b). It can be observed in Fig. 1(b) that the energetically favorable tetrahedral  $\delta a$  sites are occupied by Li. Additionally one-sixth of the octahedral  $16d$  sites are also occupied by Li at random, while the remaining five-sixths of the  $16d$  sites are occupied by Ti atoms. No obvious difference in the peak intensities and positions was found in Fig. 1(a), indicating that

the added AB did not affect the bulk crystallographic structure of  $\text{Li}_4\text{Ti}_5\text{O}_{12}$  during the heat-treatment, which is very similar with the pioneering work done by Park and co-workers.<sup>8</sup> Furthermore, the diffraction peaks of carbon had not been detected, suggesting that the residual AB is negligible and/or amorphous in the LTO-B sample. Remarkably, in spite of the identical phase structure for both samples, the samples' colors are quite different. The digital photographs of the synthetic materials display in the inset of Fig. 1 (a). It can be clearly observed that the color of LTO-B sample was blue, which is totally different from the white color for LTO-W. Apparently, Ti(III) exists in LTO-B since blue was the typical color of trivalent titanium.<sup>11</sup> Other convincing evidence will be further elaborated later.

Fig. 2 shows the typical SEM and TEM images of the LTO-B and LTO-W samples. As seen in Fig. 2 (a), the LTO-W powder revealed irregular similar spherical particles with a few obvious agglomerations where the primary particles are about 1.0  $\mu\text{m}$  in size and the secondary particles possessed a size up to 5  $\mu\text{m}$  or even larger one. This can be further confirmed by Fig. S1 (a) that shows the high-magnification SEM image of LTO-W (see Supporting Information). Conversely, as shown in Fig. 2 (b), the LTO-B powder showed a relatively uniform particle size distribution with less agglomeration. The average particle size of LTO-B was about 0.7  $\mu\text{m}$  (see Supporting Information, Fig. S1 (b)), which was significantly less than that of LTO-W. Moreover, this result was indeed confirmed by the TEM images of LTO-W and LTO-B that were showed in the inset of Fig. 2 (a) and (b), respectively. As indicated by HRTEM images shown in Fig. 2 (c) and (d), the lattice spacing of 0.487 and 0.206 nm were observed

by LTO-W and LTO-B, respectively, which were in good agreement with the  $d$ -spacing of (111) and (400) facets of the spinel  $\text{Li}_4\text{Ti}_5\text{O}_{12}$ , respectively. This further confirmed the formation of well-crystalline spinel phase in the obtained materials. Note that some disordered regions of lattice fringes were also observed in Fig. 2 (d). It may be attributed to the effect of carbothermal reduction. More importantly, based on the points discussed above, it can be concluded that the AB functioned two important roles: (i) reduced the surface Ti(IV) to Ti(III), and (ii) limited the particle-size growth of  $\text{Li}_4\text{Ti}_5\text{O}_{12}$  to some extent during the heat treatment process.<sup>27</sup> Generally speaking, the decrease of the particle size with less agglomeration can increase the utilization of the active materials, consequently enhancing the specific capacity.<sup>29</sup>

For quantifying the amount of residual carbon in the obtained materials, the thermogravimetric analysis of LTO-B and LTO-W were carried out in air. As shown in Fig. 3 (a), LTO-B powders started to lose weight slowly in air with increasing temperature, and after a slight increase the weight gradually dropped again, while the LTO-W powders remained stable over the entire temperature range. According to these observations, the weight loss of LTO-B below 120 °C could be attributed to the loss of moisture contained in the sample. In addition, the amount of residual carbon can be conveniently estimated based on the change in weight resulting from the oxidation of carbon in the range 300–500 °C.<sup>30,31</sup> The residual AB contained in the LTO-B is calculated to be 0.69 wt%, and the influence of this residual carbon on the active material can be neutralized due to the addition of 10 wt% conductive agent (AB) in the preparation of working electrode. However, it is worth mentioning that the

slight weight rise of LTO-B occurring within 120–300 °C can be ascribed to the oxidation of Ti(III), that is, the existence of Ti(III) in the as-prepared LTO-B material. Furthermore, the presence of Ti(III) on the surface of LTO-B can be further confirmed by Fig. 3 (b) that shows the high resolution Ti 2p XPS spectra of the LTO-B and LTO-W powders. Compared with the XPS spectrum of Ti 2p of LTO-W, a small negative shift can be observed in the XPS spectrum of LTO-B, indicating the Ti(III) modification on the outer surface, which is fully consistent with the previous studies on the  $\text{Li}_4\text{Ti}_5\text{O}_{12}$  system.<sup>27, 28, 32</sup> On the other hand, the lattice parameters of the obtained polycrystalline materials were determined by the least square method. For LTO-B, the lattice parameter was  $a = 8.385(2) \text{ \AA}$ , which was slightly larger than  $8.358(1) \text{ \AA}$  of LTO-W. The larger lattice parameter for the LTO-B sample is expected to occur if some of the Ti(IV) transformed to Ti(III), because of the larger ionic radius of  $\text{Ti}^{3+}$  ( $0.67 \text{ \AA}$ ) compared to  $\text{Ti}^{4+}$  ( $0.605 \text{ \AA}$ ).<sup>33</sup> In addition, the four-point D. C. test demonstrated that the electronic conductivity of LTO-B ( $1.34 \times 10^{-4} \text{ S cm}^{-1}$ ) was improved by roughly four order of magnitude than the LTO-W ( $4.03 \times 10^{-8} \text{ S cm}^{-1}$ ). More importantly, the obtained value was also relatively high when compared with those reported for the purple  $\text{Li}_4\text{Ti}_5\text{O}_{12}$  ( $1.0 \times 10^{-5} \text{ S cm}^{-1}$ ) heated under a reducing atmosphere.<sup>34, 35</sup> It indicated that the surface Ti(III) significantly enhanced electronic conductivity of the LTO-B sample due to, unlike Ti(IV), the  $\text{Ti:t}_2$  band of Ti(III) containing one electron.<sup>11</sup> Obviously, the LTO-B material with higher electronic conductivity is expected to show better electrochemical performance than the LTO-W material.

### 3.2. Lithium storage performance of the prepared electrodes

The typical galvanostatic discharge potential profiles of the LTO-W and LTO-B electrodes at the rates of 0.1 ~ 6 C over a potential window of 1.0-2.5 V are shown in Fig. 4 (a) and 4 (b), respectively. It can be clearly observed that the specific capacity for both materials gradually decreased with increasing the current rate. Furthermore, at the initial lower rate of 0.1 C, the LTO-W electrode exhibited a reversible discharge specific capacity of 160.7 mAh g<sup>-1</sup> (Fig. 4 (a)), which was slightly higher than the LTO-B of 157.3 mAh g<sup>-1</sup> (Fig. 4 (b)). This result can be mainly attributed to the slightly active material loss of the LTO-B electrode stem from the carbothermal reduction changing the surface Ti(IV) into Ti(III). However, the LTO-B delivered discharge specific capacities of 142, 126, 108 and 85 mAh g<sup>-1</sup> at current densities of 0.5, 1.0, 2.0, and 6.0 C, respectively, while at the corresponding current densities, the capacities for LTO-W were relatively low, as represented by the values of 133, 108, 83, and 49 mAh g<sup>-1</sup>. This result indicated that the surface modification of Ti(III) for Li<sub>4</sub>Ti<sub>5</sub>O<sub>12</sub> led to a significantly enhanced rate capability, which agreed well with the previous results.<sup>28</sup> Moreover, the long-term cycling performances of both samples at a high current rate of 2 C were measured as shown in Fig. 4 (c). It can be speculated that LTO-B displayed the higher capacity retention of 93.9% than that of LTO-W about 87.4%, indicating that the LTO-B electrode possessed quite excellent cyclic stability. These conclusions can be further supported by Fig. 4 (d) that gives the rate capacity and Coulombic efficiency versus cycle number of both samples. As shown in

Fig. 4 (d), the LTO-B electrode presented much higher rate capability and more excellent capacity retention than the LTO-W electrode. For instance, after 20 cycles at a current rate of 6 C, the discharge specific capacity of the LTO-B electrode was still retained 84.9 mAh g<sup>-1</sup> with negligible capacity fading, which was nearly 2 times greater than 44.8 mAh g<sup>-1</sup> of LTO-W. In addition, the Coulombic efficiencies of LTO-B electrode were also slightly higher than that of the LTO-W electrode, especially at high current rates. For example, the average Coulombic efficiency of LTO-B can reach as high as 99.7% over 20 cycles at a current rate of 2 C, which was slightly higher than 99.0% of LTO-W. Fig. 4 (e) shows the quantitative comparison of the rate capacity retention of both materials. It is quite clear that the LTO-W electrode experienced rapid capacity fading with increasing the current rate when compared with that of LTO-B electrode. From these observations, therefore, we can summarize that the Li<sub>4</sub>Ti<sub>5</sub>O<sub>12</sub> with surface modification of Ti(III) possessed improved rate capability, enhanced cyclic stability, and excellent Coulombic efficiency. The performance improvement can be mainly attributed to four reasons as follows: (i) the restraining particle-size growth of Li<sub>4</sub>Ti<sub>5</sub>O<sub>12</sub> due to the existence of AB during the sintering process; (ii) the significantly improved electrical conductivity of Li<sub>4</sub>Ti<sub>5</sub>O<sub>12</sub> owing to the surface Ti(III); (iii) the increase of the single-phase lithium insertion/extraction region because of the presence of Ti(III);<sup>8, 27</sup> (iv) the observably decreasing polarization potential resulting from the enhanced Li<sup>+</sup> diffusion coefficient of the LTO-B material (discussed later).

### 3.3. Li ions diffusion coefficients of two-phase and single-phase regions

In this research, the lithium ions diffusion coefficients of two-phase and single-phase regions in two materials were systematically determined by CV and EIS. Cyclic voltammetry (CV) is widely used to study the oxidation/reduction and/or phase transformation processes of electrode reactions and to quantitatively estimate the  $D_{\text{Li}^+}$ . Fig. 5 (a) compares the CV curves of the as-prepared LTO-B and LTO-W electrodes at a scan rate of  $0.1 \text{ mV s}^{-1}$  in the second cycle. A couple of characteristic redox peaks were observed during negative-scan and positive-scan processes that were related to the lithium insertion and extraction two-phase reactions. More importantly, the redox peak currents of the LTO-B electrode were much higher than those of the LTO-W electrode, revealing the higher electrochemical activity of LTO-B.<sup>36, 37</sup> Furthermore, the potential difference between the anodic and cathodic peaks (so-called electrochemical polarization) of the LTO-B (207 mV) was much lower than the LTO-W (304 mV), which was highly accordance with the rate discharge potential profiles of the LTO-W and LTO-B electrodes (Fig. 4 (a) and (b)). Fig. 5 (b) and (c) shows the CV curves of the LTO-B and LTO-W electrodes at different scan rates during the second cycle, respectively. It can be observed that the current and area of redox peaks for both materials increased with the increase of the scan rate. Meanwhile, the anodic peaks shifted to higher potential, and the corresponding cathodic peaks moved to lower values. It indicated that the irreversible behaviors became more obvious at higher scan rates. Moreover, the fitting results of the LTO-W and LTO-B electrodes are shown in Fig. 5 (d). The redox peak currents ( $i_p$ ) of both LTO-W and

LTO-B electrodes showed a linear relationship with the square root of scan rate ( $v^{1/2}$ ), which is due to the diffusion-limited intercalation/deintercalation processes of lithium ions. For the semi-infinite and finite diffusion, the peak current was proportional to the square root of the scan rate and can be expressed by the classical Randles-Sevchik equation:<sup>38, 39</sup>

$$i_p = 2.69 \times 10^5 n^{3/2} A C_o D_{Li^+}^{1/2} v^{1/2} \quad (1)$$

where  $n$ , the number of electrons involved in the redox reaction;  $A$ , the geometric area of electrode ( $\text{cm}^2$ );  $C_o$ , the molar concentration of lithium ions ( $\text{mol cm}^{-3}$ ),  $D_{Li^+}$ , the diffusion coefficient of lithium ions, and  $v$ , the potential scan rate ( $\text{V s}^{-1}$ ). Based on this equation, the calculated  $D_{Li^+}$  of the LTO-B and LTO-W electrodes are listed in Table 1. It was found that the  $D_{Li^+}$  of LTO-B was increased by nearly one order of magnitude when compared with that of LTO-W, which can be mainly attributed to the surface Ti(III) reducing the lithium ions diffusion barrier of  $\text{Li}_4\text{Ti}_5\text{O}_{12}$ .<sup>40-42</sup>

EIS has been considered as an effective method to determine the lithium ions diffusion coefficients, especially for the identification of the  $D_{Li^+}$  in single phase region.<sup>43</sup> As shown in Fig. 6 (a) and (b), the Li-insertion reaction regions of  $\text{Li}_{4/3}\text{Ti}_{5/3}\text{O}_4$  can be clearly distinguished by the Li-insertion depth. To be specific, the single-phase diffusion region of  $\text{Li}_{4+\delta}\text{Ti}_5\text{O}_{12}$  (or  $\text{Li}_{7-\gamma}\text{Ti}_5\text{O}_{12}$ ) can be observed at the beginning (or end) of discharge.<sup>27</sup> Conversely, in the voltage plateau region, Li-ion insertion corresponded to the two-phase ( $\text{Li}_4\text{Ti}_5\text{O}_{12}/\text{Li}_7\text{Ti}_5\text{O}_{12}$ ) conversion-reaction. Moreover, it is particularly worth mentioning that the LTO-B electrode showed an increase of single-phase diffusion region due to the presence of the surface Ti(III),

which was well consistent with the previous studies.<sup>8, 27</sup> However, to further corroborate the CV analysis results, the EIS of the LTO-W and LTO-B electrodes within single-phase region were performed upon equilibrium conditions. As marked in Fig. 6 (a) and (b), the EIS tests at the discharge potential of 1.6 V or 1.2 V (denoted as I or II) for two electrodes were carried out, and the corresponding results were showed in Fig. 6 (c). It can be seen that each Nyquist plot displayed an intercept at a high frequency, followed by a depressed semicircle in the high-middle frequency region, and a straight line in the low frequency region. Normally, the semicircle at high-middle frequency region relates to the charge-transfer resistance ( $R_{ct}$ ). As shown in Fig. 6 (c), the  $R_{ct}$  of LTO-B electrode was markedly lower than that of the LTO-W, indicating that the LTO-B electrode possessed a less electrochemical reaction polarization. Clearly, this matched well with the aforementioned results of CVs and rate-discharge curves. Moreover, the  $R_{ct}$  of both electrodes decreased with the increase of the discharge depth, suggesting that the lithium insertion gradually increased the electronic conductivity of the electrodes.<sup>31</sup> In addition, the straight line in the low frequency known as Warburg region is assigned to Li-ion diffusion within the solid-state bulk of  $\text{Li}_4\text{Ti}_5\text{O}_{12}$ .

The low frequency Warburg contribution of the impedance response has been used to determine the Li-ion diffusion coefficient in the compound.<sup>27, 43</sup> By using the model proposed by Ho et al.,<sup>44</sup> the diffusion coefficient of Li ions can be calculated as the following equation:

$$D_{Li^+} = \frac{1}{2} \left[ \left( \frac{V_M}{AF\sigma_w} \right) \frac{dE}{dx} \right]^2 \quad (2)$$

Where  $V_M$  is the molar volume of  $Li_4Ti_5O_{12}$  ( $43.94 \text{ cm}^3 \text{ mol}^{-1}$ ),  $F$  is the Faraday constant,  $A$  is the geometric area of electrode, and  $\sigma_w$  is the Warburg coefficient. The  $\sigma_w$  values at different voltages can be obtained from the slope of  $Z'$  vs.  $\omega^{-1/2}$  plots ( $\omega$  is the angular frequency) in the Warburg region. As shown in the inset of Fig. 6 (c), the  $Z'$  vs.  $\omega^{-1/2}$  plots for the low frequency Warburg region can be summarized as:

$$Z' = R + \sigma_w \omega^{-1/2} \quad (3)$$

The  $dE/dx$  is the slope of the open-circuit voltage versus mobile  $Li^+$  concentration  $x$ , which can be determined from the galvanostatic discharge curve shown in Fig. 6 (a) and (b). Thus, based on Eq. (2), the  $D_{Li^+}$  of the single-phase region in LTO-B and LTO-W were calculated and showed in Table 1. It can be seen that the  $D_{Li^+}$  values of LTO-B in single phase region were about 2 times as large as those of LTO-W, further confirming the CVs results. Namely, compared with the LTO-W material, the  $Li^+$  diffusion coefficient of the LTO-B material in single-phase region displayed improved Li-ion mobility.

As mentioned in the Introduction, the presence of Ti(III) in the insertion/extraction process of  $Li_4Ti_5O_{12}$  can increase the solid solution, consequently improving the rate capacity.<sup>8, 27</sup> However, in present work, the high rate capacity of the prepared LTO-B should be mainly attributed to the observably decreased electrochemical polarization, not only originating from the significantly improved electronic conductivity but also arising from the enhanced  $Li^+$  diffusion coefficient. Undoubtedly, the increase of solid solution plays a less important role. This

conclusion is of importance since it provides a new perspective to identify the real role of Ti(III). With this view, therefore, we tend to believe that the carbothermal reduction method is an ideal choice for facile synthesis of  $\text{Li}_4\text{Ti}_5\text{O}_{12}$  with simultaneously improved the electronic and ionic conductivity.

### 3.4. Formation mechanism of the carbothermal reduction method

It is generally known that rutile is the only stable phase of coarse grained titania, whereas anatase and brookite are metastable at all temperatures and easily convert to rutile when heated.<sup>45, 46</sup> The pristine  $\text{Li}_2\text{CO}_3$  melts at 723 °C, and decomposes in air at 1310 °C under atmospheric pressure.<sup>47</sup> However, heating of  $\text{Li}_2\text{CO}_3$  in the presence of  $\text{TiO}_2$  in air is known to expel  $\text{CO}_2$  at temperatures as low as 700 °C,<sup>48</sup> leading to complex oxide formation such as  $\text{Li}_4\text{TiO}_4$ ,<sup>49</sup> or  $\text{Li}_2\text{TiO}_3$ <sup>50</sup> depending on molar ratios of mixtures and types of atmosphere (air, Ar, Ar/ $\text{H}_2$ ). Furthermore, during the preparation of the surface modified  $\text{Li}_4\text{Ti}_5\text{O}_{12}$ , the previous studies have demonstrated that the decomposed and melted lithium salt ( $\text{Li}_2\text{O}$ ) can diffuse through the pre-coating of carbon or polymer layer to react with  $\text{TiO}_2$  precursor during high temperature annealing.<sup>17, 27, 51</sup> Therefore, in view of all these factors, the formation process of  $\text{Li}_4\text{Ti}_5\text{O}_{12}$  with surface modification of Ti(III) by carbothermal reduction method was discreetly clarified as shown in Scheme 1. It was clear that the formation process was strictly divided into five steps as follows: (i) the gradual transformation of anatase into rutile with the increase of temperature; (ii) the grain boundary growth with the increasing amount of rutile;<sup>47</sup> (iii) the decomposition and fusion of  $\text{Li}_2\text{CO}_3$ ;

(iv) the diffusion reaction generation of  $\text{Li}_4\text{Ti}_5\text{O}_{12}$  under the continuous high-temperature condition; (v) the surface reduction of  $\text{Li}_4\text{Ti}_5\text{O}_{12}$  due to the carbon reducibility at high temperature. In fact, the XRD analysis indicated that the synthetic product at 750 °C for 12 h in flowing argon contained the spinel  $\text{Li}_4\text{Ti}_5\text{O}_{12}$  phase, however, the color of the obtained material did not change (not shown here), suggesting that the surface reduction process is restricted by the sintering temperature. This is expected to happen if we considered the possibility of thermodynamics, because the reduction strength of carbon hardly conquers the high bond energy of  $\text{TiO}_6$  octahedral unless providing sufficiently high temperature. In our case, this critical temperature was not less than 800 °C. Additionally, it was worth mentioning that the aforementioned five steps may overlap, viz., the two consecutive steps were likely to occur simultaneously. The purpose of this compulsory partition was to facilitate understanding of the essential formation process.

#### 4. Conclusions

The present work introduced a simple cost-saving carbothermal reduction method to design  $\text{Li}_4\text{Ti}_5\text{O}_{12}$  anode with surface modification of Ti(III) using anatase- $\text{TiO}_2$ ,  $\text{Li}_2\text{CO}_3$ , and acetylene black (AB) as precursors. Remarkably, this seemingly ordinary design can tactfully eliminate the influence of residual carbon, and thus make it possible to individually study the effect of Ti(III) on bulk  $\text{Li}_4\text{Ti}_5\text{O}_{12}$ . According to the test results of the physicochemical and electrochemical performance, a new

perspective was proposed to understand the real role of Ti(III). The presence of Ti(III) on the surface of  $\text{Li}_4\text{Ti}_5\text{O}_{12}$  not only significantly improves the electronic conductivity, but also enhances the  $\text{Li}^+$  diffusion coefficient, thus observably decreasing electrochemical polarization and improving the rate performance of the obtained material. Therefore, it is believed that the carbothermal reduction method is an ideal choice for facile synthesis of  $\text{Li}_4\text{Ti}_5\text{O}_{12}$  with simultaneously improved electronic and ionic conductivity. More importantly, the carbothermal reduction mechanism was illustrated, which may be very beneficial to the development of novel  $\text{Li}_4\text{Ti}_5\text{O}_{12}$  material for commercial applications.

### **Acknowledgment**

This work was financially supported by the National Natural Science Foundation of China (No. 51164006, 51472180 and 51272176), Key Project of Tianjin Municipal Natural Science Foundation of China (14JCZDJC32200 and 13JCZDJC33900), LPMT, CAEP (KF14006), Academic Innovation Funding of Tianjin Normal University (52XC1404), Scientific Research Foundation for Returned Overseas Chinese Scholars of State Education Ministry, and the program of Thousand Youth Talents in Tianjin of China.

### **Reference**

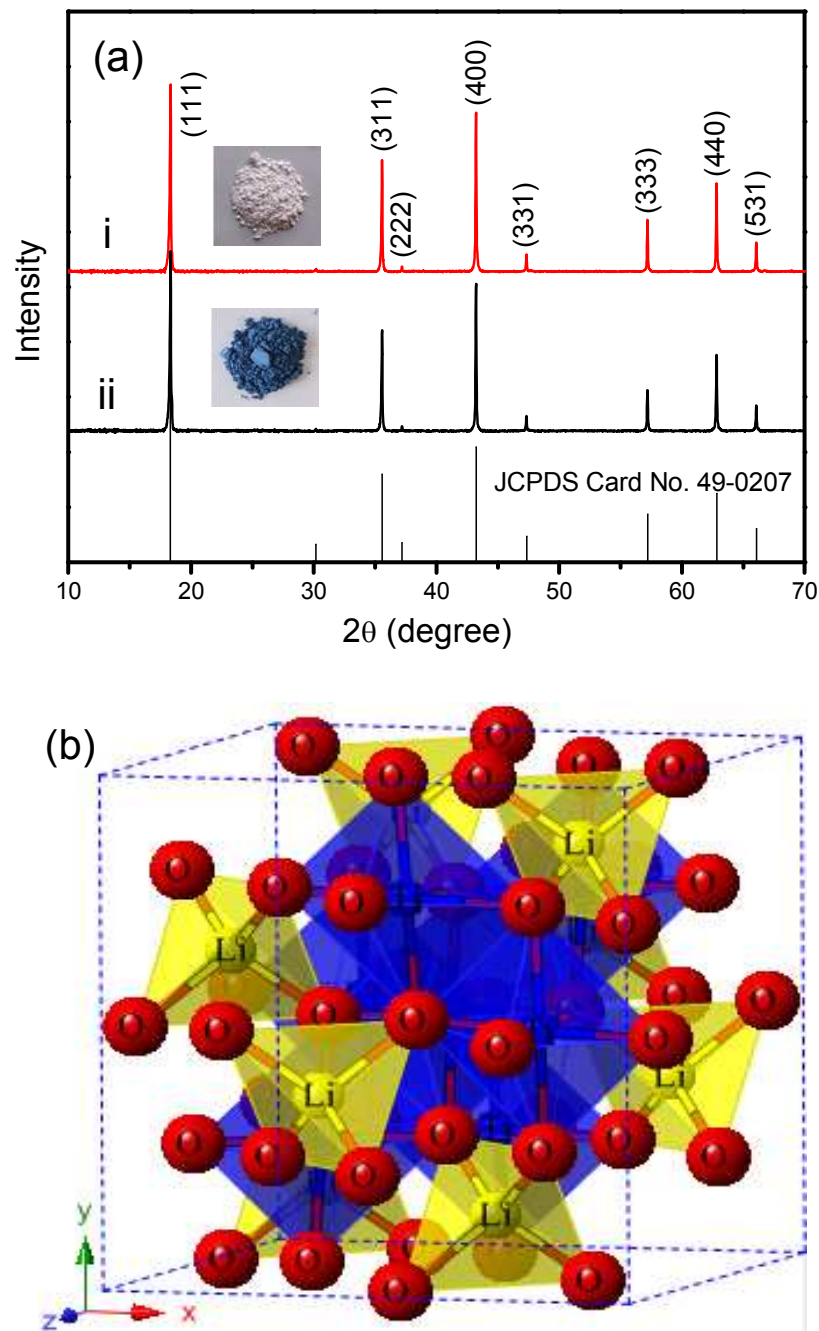
- 1 J. M. Tarascon and M. Armand, *Nature*, 2001, **414**, 359–367.
- 2 C. Z. Yuan, H. B. Wu, Y. Xie and X. W. Lou, *Angew. Chem. Int. Ed.*, 2014, **53**, 1488–1504.
- 3 R. V. Noorden, *Nature*, 2014, **507**, 26–28.
- 4 J. Jiang, Y. Y. Li, J. P. Liu, X. T. Huang, C. Z. Yuan and X. W. Lou, *Adv. Mater.*, 2012, **24**, 5166–5180.
- 5 A. Manthiram, *J. Phys. Chem. Lett.*, 2011, **2**, 176–184.
- 6 G. Q. Zhang, B. Y. Xia, C. Xiao, L. Yu, X. Wang, Y. Xie and X. W. Lou, *Angew. Chem. Int. Ed.*, 2013, **52**, 8643–8647.
- 7 B. K. Guo, X. Q. Wang, P. F. Fulvio, M. F. Chi, S. M. Mahurin, X. G. Sun and S. Dai, *Adv. Mater.*, 2011, **23**, 4661–4666.
- 8 K. S. Park, A. Benayad, D. J. Kang and S. G. Doo, *J. Am. Chem. Soc.*, 2008, **130**, 14930–14931.
- 9 Z. H. Chen, Y. Qin, Y. Ren, W. Q. Lu, C. Orendorff, E. P. Roth and K. Amine, *Energy Environ. Sci.*, 2011, **4**, 4023–4030.
- 10 K. Amine, I. Belharouak, Z. H. Chen, T. Tran, H. Yumoto, N. Ota, S. T. Myung and Y. K. Sun, *Adv. Mater.*, 2010, **22**, 3052–3057.
- 11 K. M. Colbow, J. R. Dahn and R. R. Haering, *J. Power Sources*, 1989, **26**, 397–402.
- 12 T. Ohzuku, A. Ueda and N. Yamamoto, *J. Electrochem. Soc.*, 1995, **142**, 1431–1435.
- 13 G. G. Amatucci, F. Badway, A. Du Pasquier and T. Zheng, *J. Electrochem. Soc.*,

- 2001, **148**, A930–A939.
- 14 C. H. Chen, J. T. Vaughey, A. N. Jansen, D. W. Dees, A. J. Kahaian, T. Goacher and M. M. Thackeray, *J. Electrochem. Soc.*, 2001, **148**, A102–A104.
- 15 Y. K. Sun, D. J. Jung, Y. S. Lee and K. S. Nahm, *J. Power Sources*, 2004, **125**, 242–245.
- 16 H. G. Jung, S. T. Myung, C. S. Yoon, S. B. Son, K. H. Oh, K. Amine, B. Scrosati and Y. K. Sun, *Energy Environ. Sci.*, 2011, **4**, 1345–1351.
- 17 G. N. Zhu, H. J. Liu, J. H. Zhuang, C. X. Wang, Y. G. Wang and Y. Y. Xia, *Energy Environ. Sci.*, 2011, **4**, 4016–4022.
- 18 Y. Qi, Y. Huang, D. Jia, S. J. Bao and Z. P. Guo, *Electrochim. Acta*, 2009, **54**, 4772–4776.
- 19 L. F. Shen, C. Z. Yuan, H. J. Luo, X. G. Zhang, S. D. Yang and X. J. Lu, *Nanoscale*, 2011, **3**, 572–574.
- 20 Y. Shi, L. Wen, F. Li and H. M. Cheng, *J. Power Sources*, 2011, **196**, 8610–8617.
- 21 S. H. Huang, Z. Y. Wen, X. J. Zhu and Z. H. Gu, *Electrochem. Commun.*, 2004, **6**, 1093–1097.
- 22 Z. M. Liu, N. Q. Zhang, Z. J. Wang and K. N. Sun, *J. Power Sources*, 2012, **205**, 479–482.
- 23 L. Yu, H. B. Wu and X. W. Lou, *Adv. Mater.*, 2013, **25**, 2296–2300.
- 24 M. Wagemaker, D. R. Simon, E. M. Kelder, J. Schoonman, C. Ringpfeil, U. Haake, D. Lützenkirchen-Hecht, R. Frahm and F. M. Mulder, *Adv. Mater.*, 2006, **18**, 3169–3173.

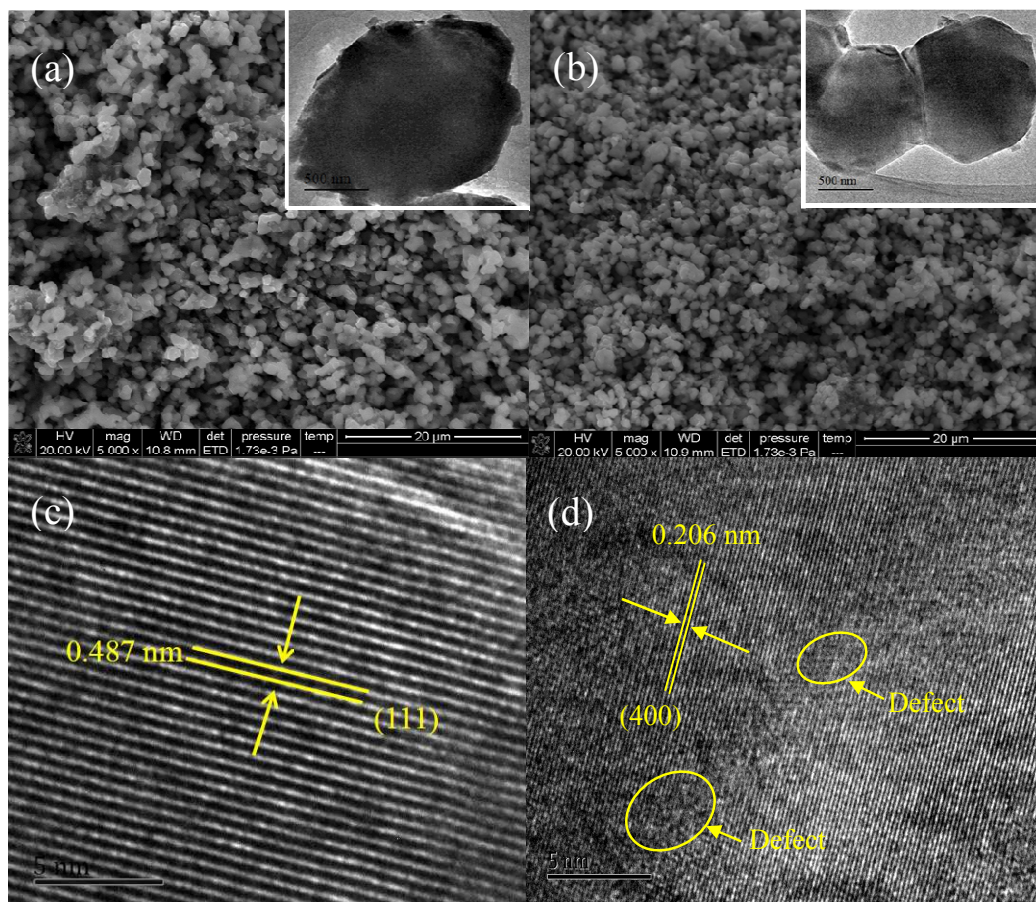
- 25 M. Wagemaker, E. R. H. van Eck, A. P. M. Kentgens and F. M. Mulder, *J. Phys. Chem. B*, 2009, **113**, 224–230.
- 26 P. Gibot, M. Casas-cabanas, L. Laffont, S. Levasseur, P. Carlach, S. Hamelet, J. M. Tarascon and C. Masquelier, *Nat. Mater.*, 2008, **7**, 741–747.
- 27 Y. G. Wang, H. M. Liu, K. X. Wang, H. Eiji, Y. Wang and H. S. Zhou, *J. Mater. Chem.*, 2009, **19**, 6789–6795.
- 28 Z. N. Wan, R. Cai, S. M. Jiang and Z. P. Shao, *J. Mater. Chem.*, 2012, **22**, 17773–17781.
- 29 K. X. Wang, X. H. Li and J. S. Chen, *Adv. Mater.*, DOI: 10.1002/adma.201402962.
- 30 M. M. Rahman, J. Z. Wang, M. F. Hassan, D. Wexler and H. K. Liu, *Adv. Energy Mater.*, 2011, **1**, 212–220.
- 31 J. W. Yang, B. Yan, J. Ye, X. Li, Y. S. Liu and H. P. You, *Phys. Chem. Chem. Phys.*, 2014, **16**, 2882–2891.
- 32 L. F. Shen, E. Uchaker, X. G. Zhang and G. Z. Cao, *Adv. Mater.*, 2012, **24**, 6502–6506.
- 33 X. M. Chen, X. F. Guan, L. P. Li and G. S. Li, *J. Power Sources*, 2012, **210**, 297–302.
- 34 J. Wolfenstine, U. Lee and J. L. Allen, *J. Power Sources*, 2006, **154**, 287–289.
- 35 J. Wolfenstine and J. L. Allen, *J. Power Sources*, 2008, **1**, 582–585.
- 36 A. L. M. Reddy, M. M. Shaijumon, S. R. Gowda and P. M. Ajayan, *Nano Lett.*, 2009, **9**, 1002–1006.

- 37 Y. W. Li, J. H. Yao, E. Uchaker, M. Zhang, J. J. Tian, X. Y. Liu and G. Z. Cao, *J. Phys. Chem. C*, 2013, **117**, 23507–23514.
- 38 J. R. Dahn, J. W. Jiang, L. M. Moshurchak, M. D. Fleischauer, C. Buhrmester and L. J. Krause, *J. Electrochem. Soc.*, 2005, **152**, A1283–A1289.
- 39 H. Liu, L. J. Fu, H. P. Zhang, J. Gao, C. Li, Y. P. Wu and H. Q. Wu, *Electrochem. Solid-State Lett.*, 2006, **9**, A529–A533.
- 40 M. V. Koudriachova, N. M. Harrison and S. M. de Leeuw, *Phys. Rev. Lett.*, 2001, **86**, 1275–1278.
- 41 S. P. Ong, V. L. Chevrier, G. F. Hautier, A. Jain, C. Moore, S. Kim, X. H. Ma and G. Ceder, *Energy Environ. Sci.*, 2011, **4**, 3680–3688.
- 42 M. Wagemaker and F. M. Mulder, *Acc. Chem. Res.*, 2012, **46**, 1206–1215.
- 43 Y. H. Rho and K. Kanamura, *J. Solid State Chem.*, 2004, **177**, 2094–2100.
- 44 C. Ho, I. D. Raistrick and R. A. Huggins, *J. Electrochem. Soc.*, 1980, **127**, 343–350.
- 45 J. F. Banfield, D. R. Veblen and D. J. Smith, *Am. Mineral.*, 1991, **76**, 343–353.
- 46 G. Madras, B. J. McCoy and A. Navrotsky, *J. Am. Ceram. Soc.*, 2007, **90**, 250–255.
- 47 J. A. Mergos and C. T. Dervos, *Mater. Charact.*, 2009, **60**, 848–857.
- 48 G. Izquierdo and A. R. West, *Mater. Res. Bul.*, 1980, **15**, 1655–1660.
- 49 N. Togashi, T. Okumura and K. Oh-ishi, *J. Ceram. Soc. Japan*, 2007, **115**, 324–328.
- 50 A. Deschanvres, B. Raveau and Z. Sekkal, *Mater. Res. Bul.*, 1971, **6**, 699–704.

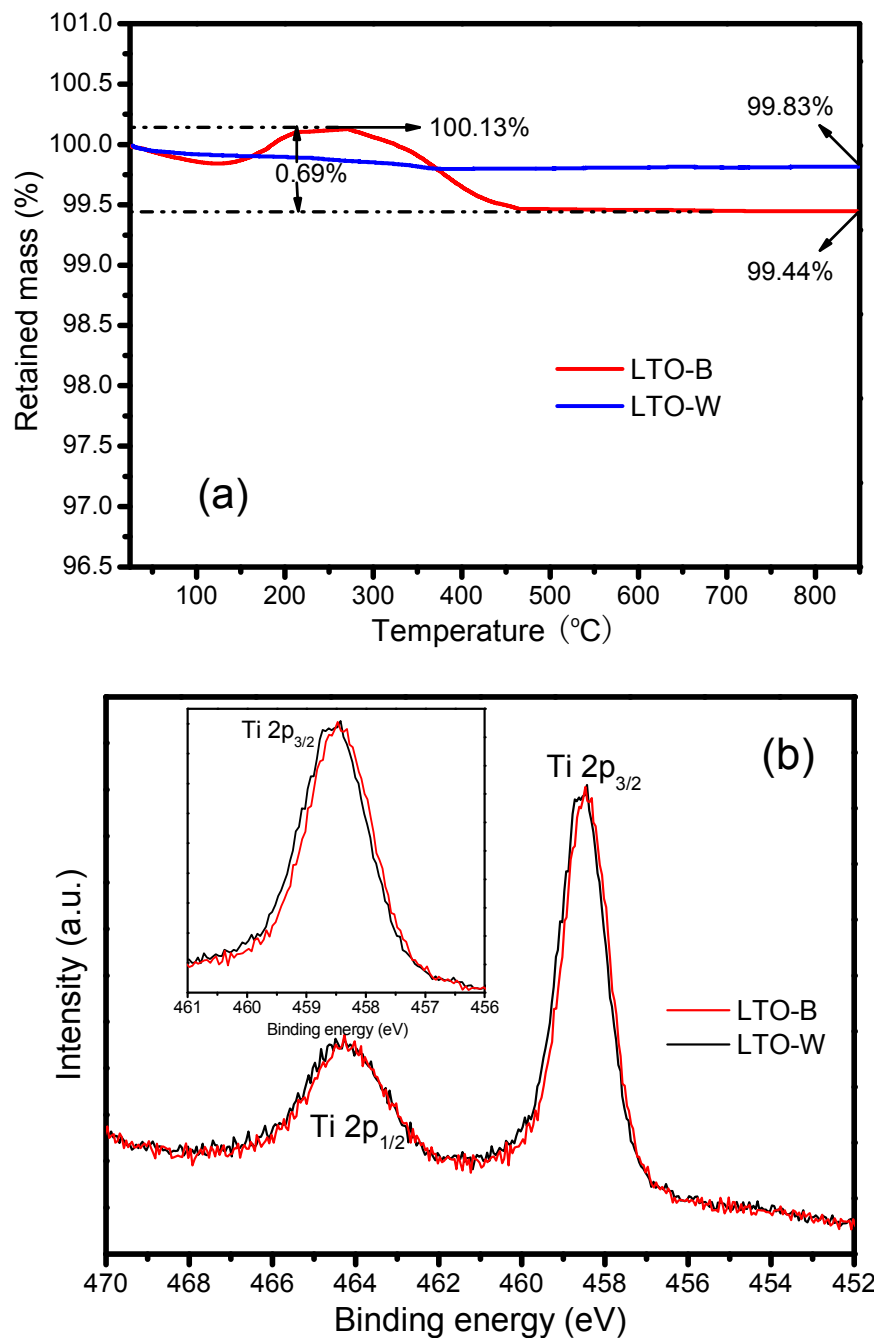
- 51 L. Cheng, J. Yan, G. N. Zhu, J. Y. Luo, C. X. Wang and Y. Y. Xia, *J. Mater. Chem.*, 2010, **20**, 595–602.



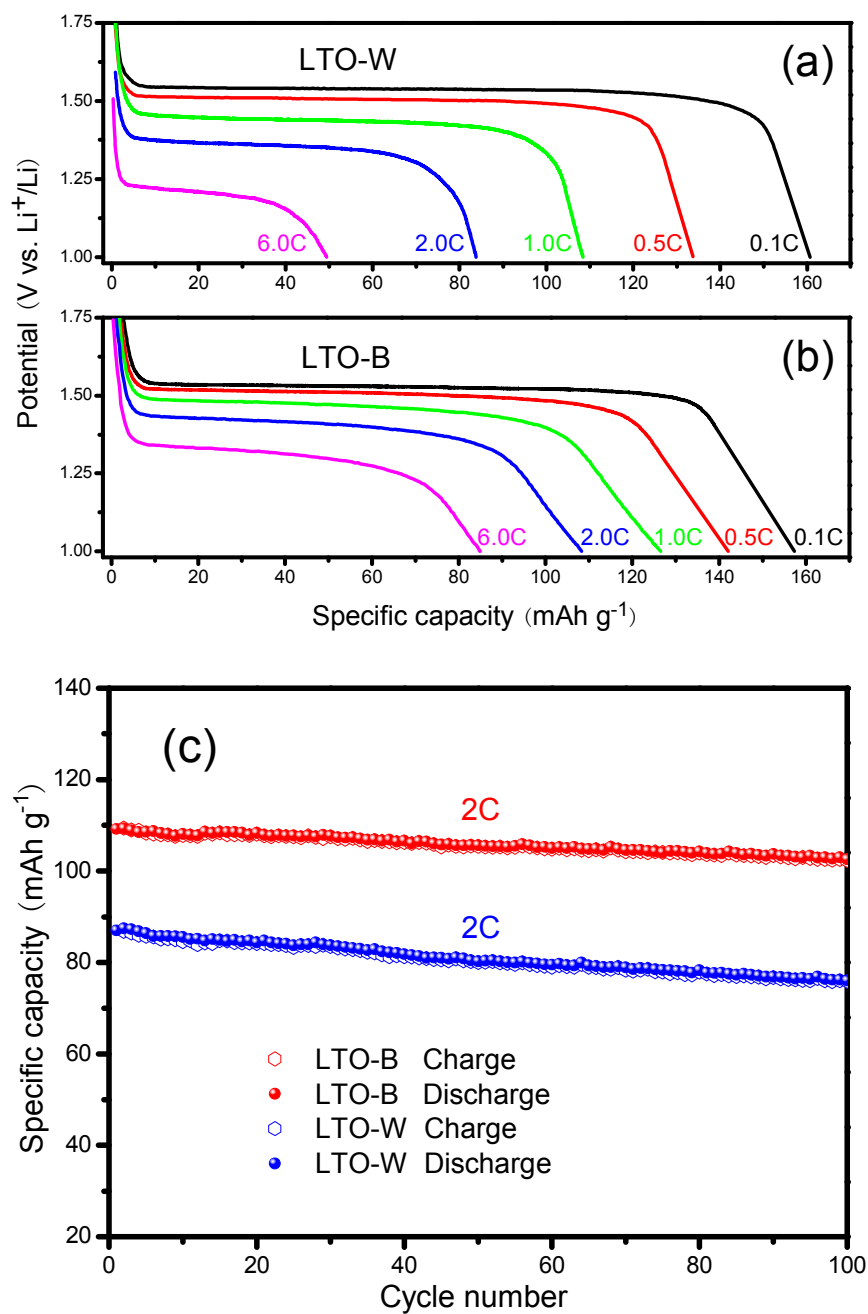
**Fig. 1** (a) XRD patterns of the materials: i) LTO-W and ii) LTO-B. Insets show the corresponding powder colors. The vertical lines on the x-axis correspond to the standard XRD reflections of spinel  $\text{Li}_4\text{Ti}_5\text{O}_{12}$ . (b) The cubic crystalline structure of spinel  $\text{Li}_4\text{Ti}_5\text{O}_{12}$ .

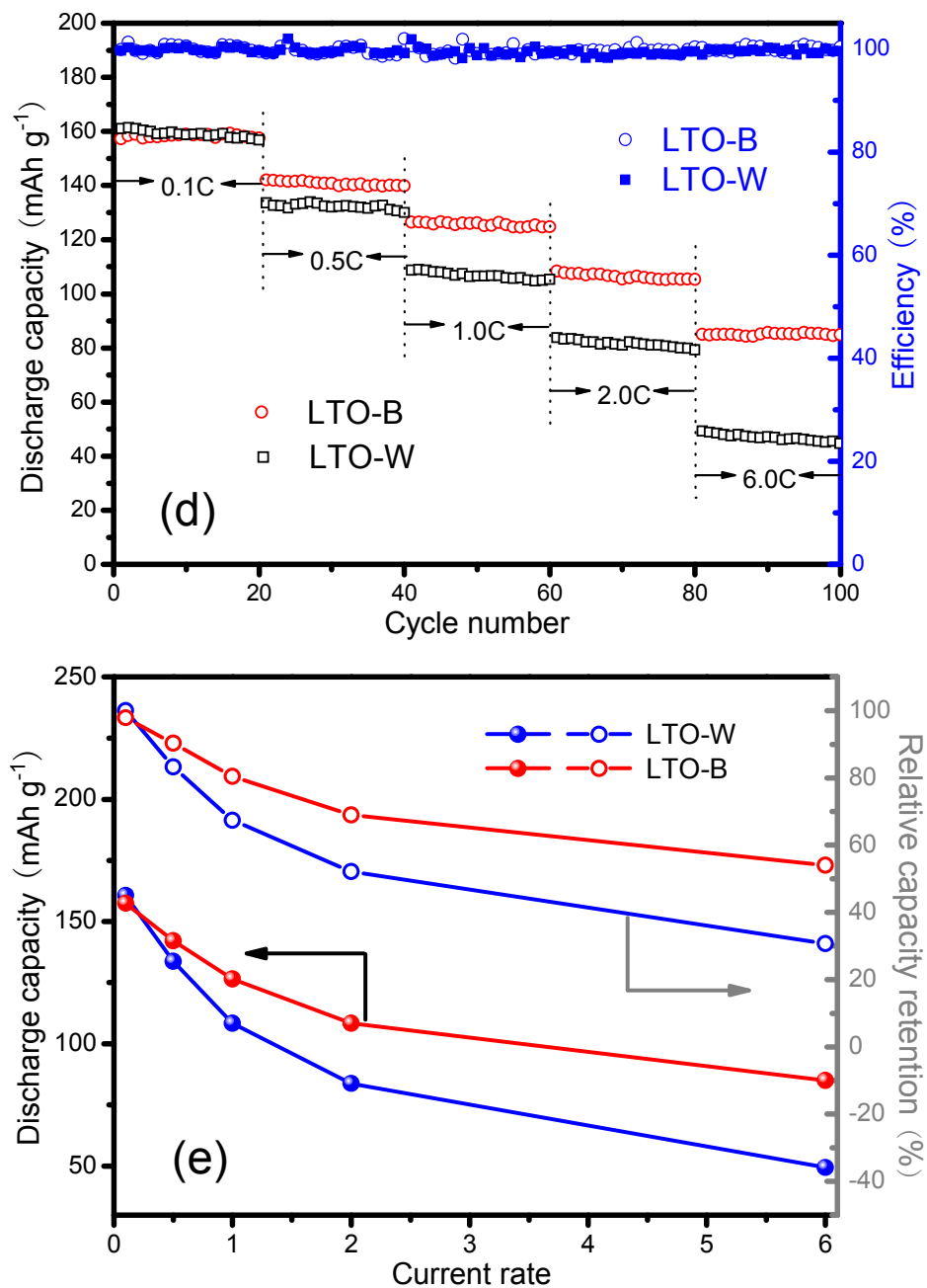


**Fig. 2** SEM images of (a) LTO-W and (b) LTO-B. Inset: the corresponding TEM images of the LTO-W and LTO-B. HRTEM images for (c) LTO-W and (d) LTO-B.

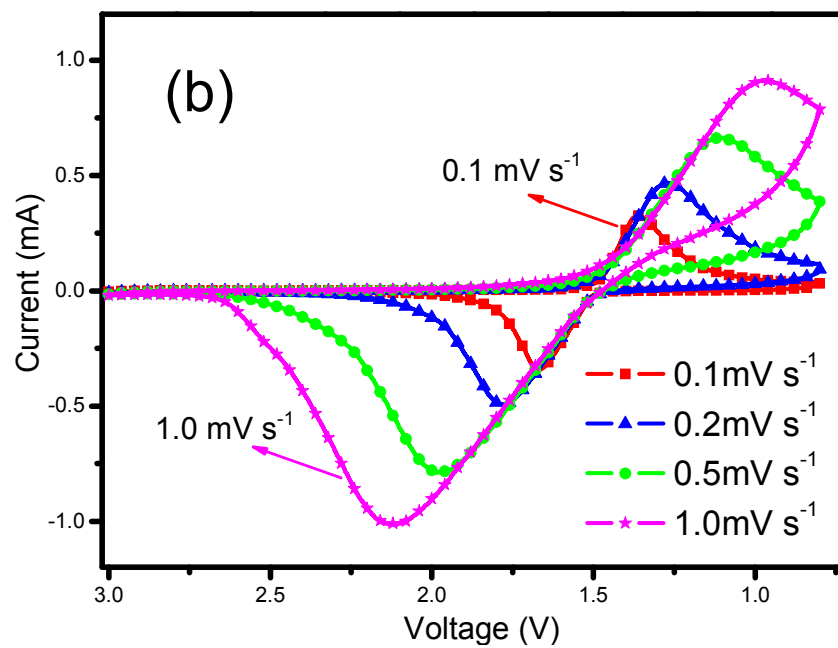
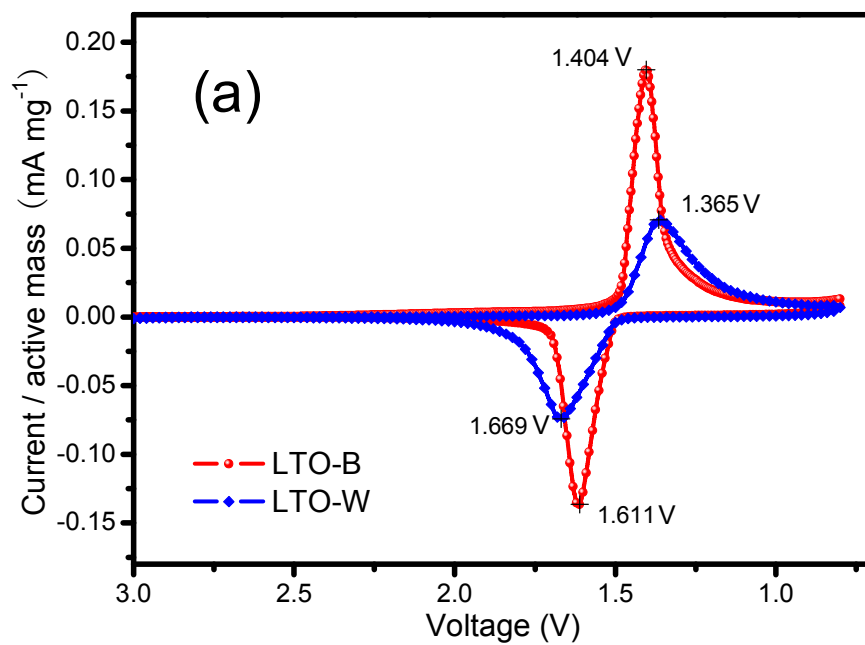


**Fig. 3** (a) TGA curves of LTO-W and LTO-B powder samples; (b) high resolution XPS spectra of Ti 2p for LTO-W and LTO-B.





**Fig. 4** Galvanostatic discharge voltage profiles at different current rates of (a) LTO-W and (b) LTO-B; (c) the long-term cycling performances of LTO-W and LTO-B at a high current rate of 2 C; (d) discharge capacity and Coulombic efficiency versus cycle number; (e) comparison of the capacity retention.



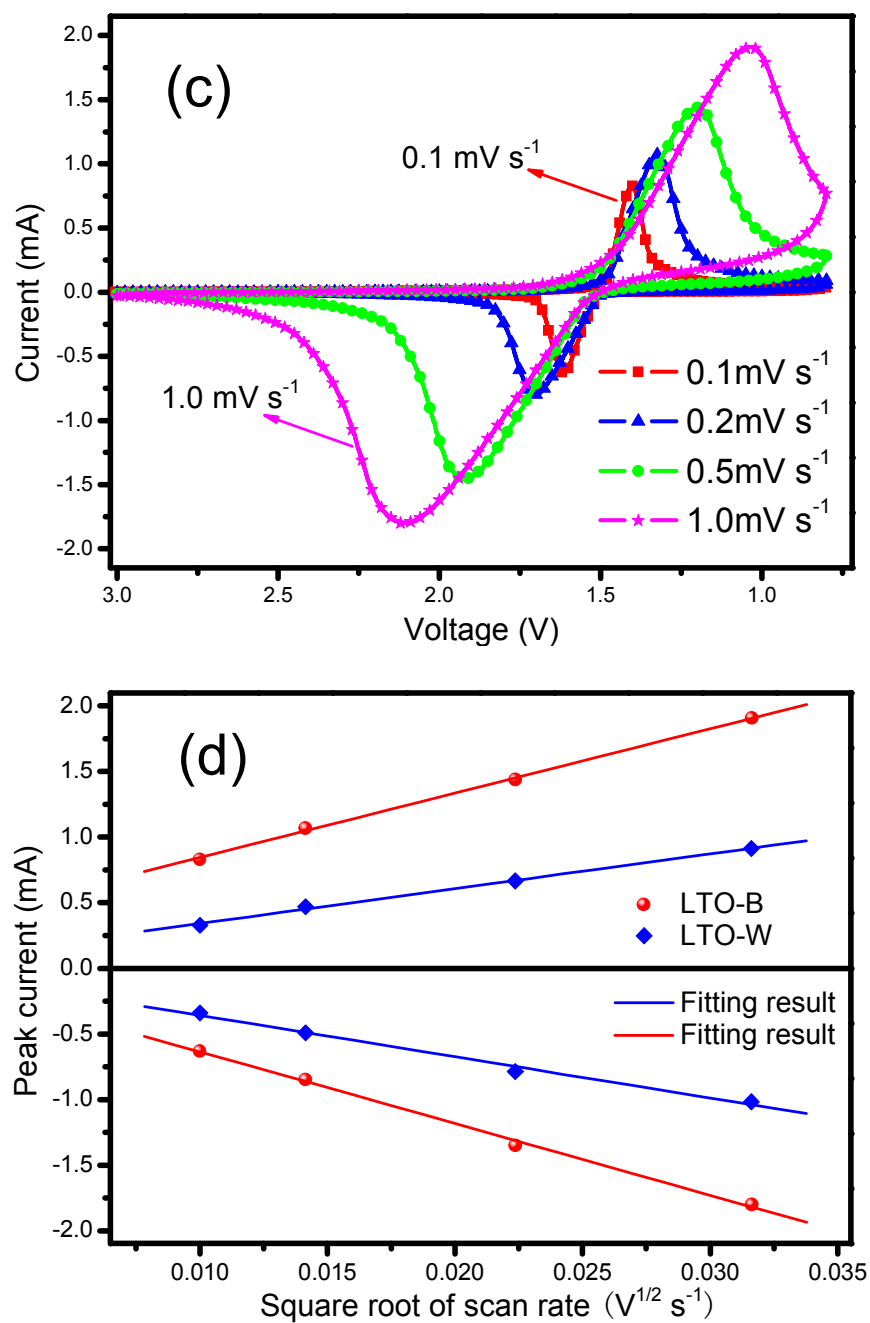


**Fig. 5** (a) CV curves of LTO-W and LTO-B electrodes at the second cycle with scan rate of 0.1 mV s<sup>-1</sup>; CV curves at different scan rates of (b) LTO-W and (c) LTO-B; (d) relationship of the peak current ( $i_p$ ) and the square root of scan rate ( $v^{1/2}$ ).

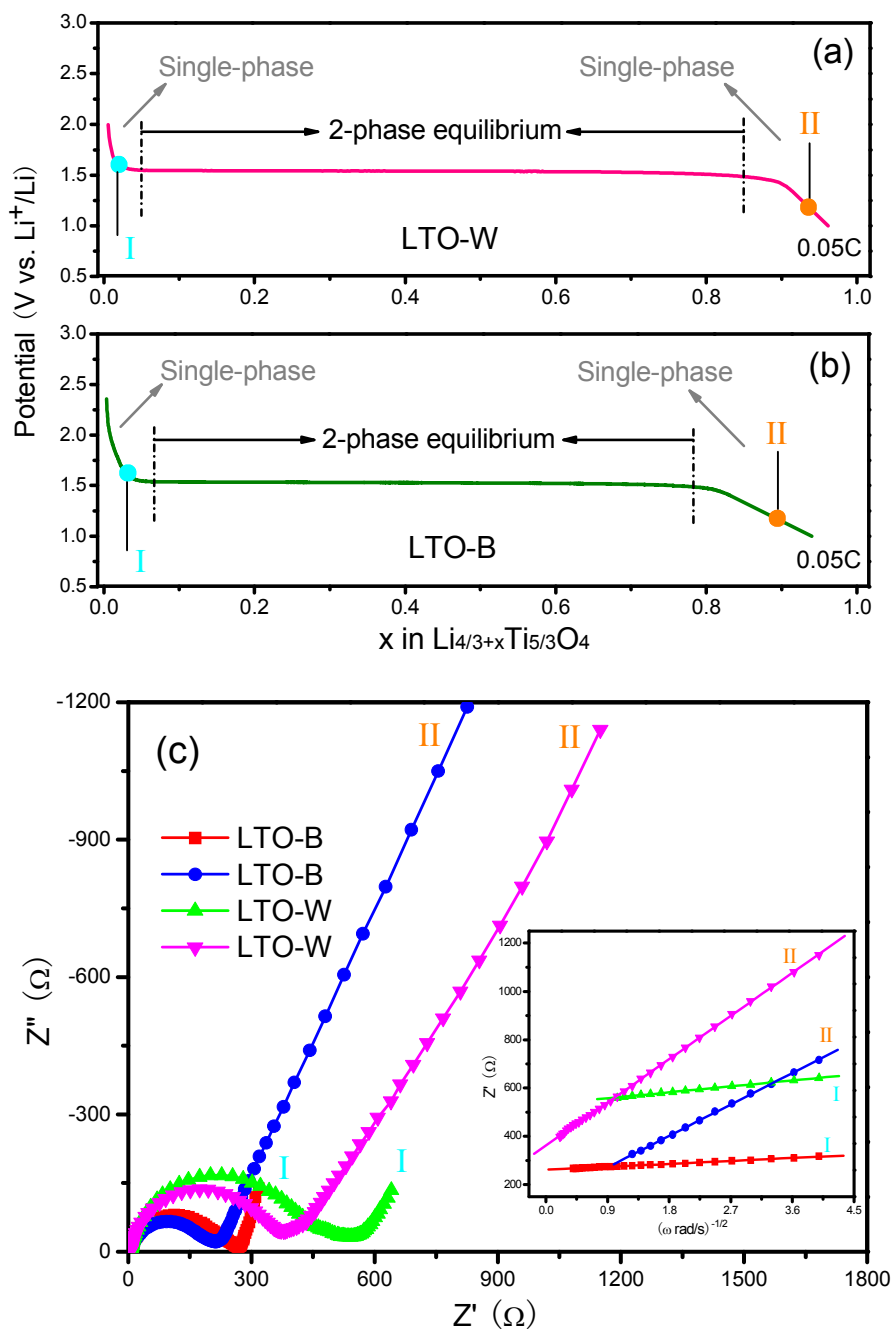
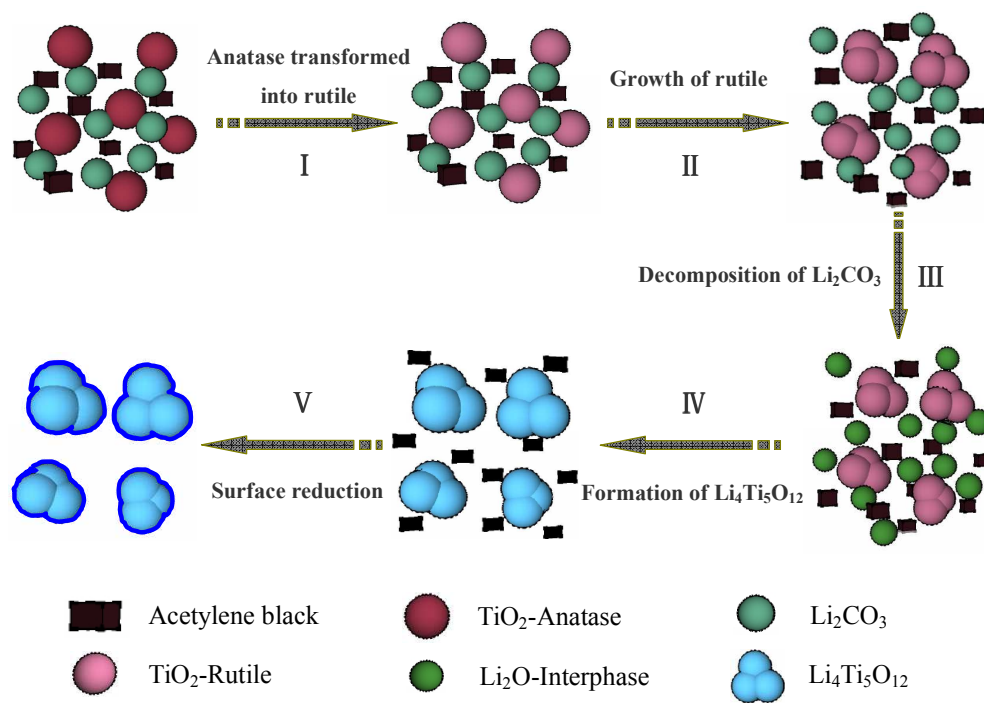
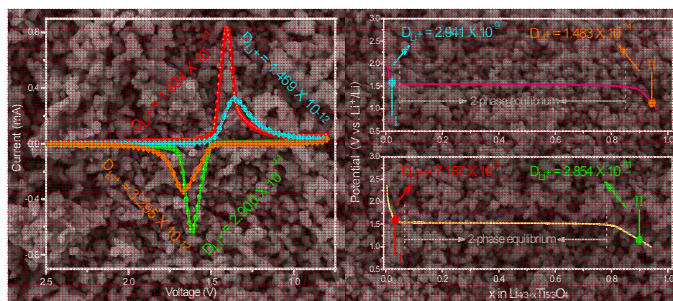


**Fig. 6** Electrochemical voltage-composition curves for (a) LTO-W and (b) LTO-B vs. Li at a current rate of 0.05 C during the second cycle; (c) the Nyquist plots under different discharge state for the single-phase region of LTO-W and LTO-B. Inset shows the plots of the real part of impedance as a function of the inverse square root of angular frequency in the Warburg region.



**Scheme 1** The formation mechanism of carbothermal reduction for LTO-B.

## Graphical Abstract



The electronic and ionic conductivity of  $\text{Li}_4\text{Ti}_5\text{O}_{12}$  can be simultaneously improved via a facile cost-saving carbothermal reduction method.

**Table 1.** The lithium-ion diffusion coefficients of LTO-B and LTO-W electrodes calculated from CV and EIS.

$D_{Li^+}$ (cm <sup>2</sup> s <sup>-1</sup> )	two-phase region		single-phase region	
	Li-insertion	Li-extraction	I (1.6 V)	II (1.2 V)
LTO-B	$1.834 \times 10^{-11}$	$2.900 \times 10^{-11}$	$7.187 \times 10^{-9}$	$2.854 \times 10^{-11}$
LTO-W	$1.469 \times 10^{-12}$	$3.295 \times 10^{-12}$	$2.941 \times 10^{-9}$	$1.483 \times 10^{-11}$